9-2020

Large-stroke capacitive MEMS accelerometer without pull-in

Meysam Daeichin
Binghamton University--SUNY, mdaeich1@binghamton.edu

Ronald Miles
Binghamton University--SUNY, rmiles@binghamton.edu

Shahrzad Towfighian
Binghamton University--SUNY, stowfigh@binghamton.edu

Large-stroke capacitive MEMS accelerometer without pull-in

Meysam Daeichin, Ronald N. Miles, and Shahrzad Towfighian

***Abstract*— In this study, the feasibility of obtaining electrical read-out data from a capacitive MEMS accelerometer that employs repulsive electrode configuration is demonstrated. This configuration allows for large-stroke vibrations of microstructures without suffering from pull-in failure that exists in conventional accelerometers based on the parallel-plate configuration. With initial fabrication gap of 2.75μm, the accelerometer can reach a 4.2μm dynamical displacement amplitude. The accelerometer is tested up to $95(\mathrm{V})$ without exhibiting pull-in failure. For comparison, the pull-in voltage of an accelerometer with same dimensions but with conventional parallel-plate electrode configuration is $0.8(\mathrm{V})$. The MEMS device is fabricated using the POLYMUMPs fabrication standard. An electrical circuit is built to measure the capacitance change due to motion of the accelerometer proof-mass. The accelerometer has a mechanical sensitivity of $35\frac{\mathrm{nm}}{\mathrm{g}}$ and electrical sensitivity of $5.3\frac{\mathrm{mV}}{\mathrm{g}}$. The ability to use large bias voltages without the typical adverse effects on the stability of the moving electrode will enable the design of capacitive MEMS accelerometers with enhanced resolution and tunable frequency range.**

***Index Terms*— Electrical read-out, MEMS accelerometer, Repulsive electrode configuration**

I. Introduction

The first micromachined accelerometer was developed in the late 1970s based on the piezoresistive effect and a bulk micromachining process [1]. Since then, accelerometers based on different sensing methods and fabrication techniques have been introduced [2]. For example, piezoelectric, thermal, optical, capacitive, and tunneling accelerometers have been developed and fabricated with fabrication techniques such as bulk and surface micromachining [2]. Today, the most common accelerometer, especially in automotive and consumer electronic applications, is the capacitive accelerometer fabricated with surface micromachining [2]. Capacitive accelerometers offer high sensitivity, low power consumption, low sensitivity to changes in temperature, low fabrication cost, and ease of integration with CMOS technology [2], [3].

In a previous work, we presented the mechanical characterization of a rotational accelerometer that employed the repulsive electrode configuration [4]. In this study, we extend the work to demonstrate the feasibility of getting an electrical read-out from an accelerometer that uses the repulsive electrode configuration. To achieve this goal, we have developed a system that allows for measuring the electrical output of the accelerometer when it is subjected to mechanical excitation. An electrical circuit is designed and built for measuring the change in the capacitance in the proposed accelerometer. This paper describes the challenges we overcame to measure the electrical output of the proposed accelerometer. The current design of the accelerometer is an improvement over a previous design that had a rotational degree of freedom. The current design leads to less residual stress in the microstructure from the fabrication process because of the use of serpentine springs for supporting the proof-mass. Moreover, the current design increases the number of electrodes by 25 % because they can be employed over all four sides of the proof-mass. In the previous design, the electrodes could be employed on only three sides of the proof-mass.

Capacitive MEMS accelerometers were developed in the late 80s and early 90s by Analog Devices Inc. (ADXL50 accelerometer) and Motorola [5]. Their design basically has not been changed since then. They typically consist of two electrodes with a voltage difference applied between them, with one electrode moving and one fixed. They usually come in two design flavors, parallel-plate and interdigitated electrodes [2]. In surface micromachining, the in-plane dimensions can be from a few microns to a few millimeters whereas the thicknesses are in the range of a few microns [2]. Because of this, the parallel-plate design is usually used for sensing acceleration in the vertical directions, and the interdigitated-electrodes design is used for in-plane acceleration sensing. The common theme between these two designs is that the electrostatic force always pulls the moving electrode toward the fixed electrode. This leads to the pull-in instability problem [6]. Pull-in happens where the restoring

This manuscript is submitted for review on May 30, 2020. The authors would like to acknowledge the financial support of this study by the National Science Foundation (NSF) through grant #ECCS1608692. The authors would like to thank Dr. Hassan Hosseinpor for his help with this project.

Meysam Daeichin (mdaeich1@binghamton.edu), Ronald N. Miles(miles@binghamton.edu), and Shahrzad Towfighian (stowfigh@binghamton.edu) (Corresponding author) are with the Department of Mechanical Engineering in State University of New York at Binghamton.

force of the flexible element(s) of the microstructure is no longer able to resist the electrostatic force on the moving electrode [3]. Therefore, the moving electrode collapses to the fixed electrode causing the permanent failure of the MEMS device. The pull-in instability imposes a limitation on the travel range of the moving electrode that is not desirable. Usually the safe travel range is one third of the initial fabrication gap between the moving and fixed electrodes. These problems exist in almost all the capacitive MEMS sensors and actuators based on the two-electrode design approach. A MEMS transducer that is robust against pull-in instability and or has a large stable travel range is very desirable [7].

There have been numerous methods proposed in the literature to eliminate or mitigate the pull-in instability and extend the travel range of the moving electrode. These methods generally fall into three categories: modifying the restoring force of the microstructure, changing the electrostatic force on the moving electrode, and introducing mechanical stoppers to prevent the collapse of the moving electrode to the fixed electrode. For instance, piece-wise linear or nonlinear springs [8] are proposed to strengthen the restoring force of the microstructure, and therefore extending the safe stable travel range. However, these methods do not eliminate the pull-in instability but just mitigate it. Closed-loop voltage control [9] is a method to get feedback from the displacement of the moving electrode to change the bias voltage between the two electrodes. This method basically modifies the electrostatic force by changing the voltage and extend the stable travel range. This method adds complexity to the electrical circuitry. Adding another constant capacitor in series with the variable capacitor [10] is another method to modify the electrostatic force and extend the stable region for the microstructure. This method is equivalent to enlarging the initial fabrication gap and thus does not eliminate the pull-in instability completely. The added capacitor introduces parasitic capacitance, which degrades the device performance. Charge or current control [11], [12] and leveraged bending [13] are among the other methods to extend the stable region. Especially, in the leverage bending approach, it is possible to achieve 100% of the initial gap as the stable travel range for microstructures such as cantilever and clamped-clamped beams.

Another approach toward capacitive transduction is using the repulsive electrode configuration [14], [15]. In this approach, instead of two electrodes (one fixed and one moving) there are four electrodes. Three of the electrodes are fixed on the substrate, and the forth one is the moving electrode suspended above the middle fixed electrode. Figure 1 shows the schematic of this electrode configuration and voltage distribution in the repulsive scheme. In the repulsive configuration, an electrical voltage is applied on the two side electrodes on the substrate, while the middle fixed electrode and the moving electrode are grounded. This voltage distribution leads to an electrostatic force that pushes the moving electrode away from the substrate [16], [17]. This nature of the electrostatic force eliminates the pull-in possibility between the moving electrode and the underlying fixed electrode [4], [15], [18]. Aside from eliminating pull-in, another advantage of the repulsive approach is that it extends the travel range of the microstructure more than initial fabrication gap and therefore provides a transduction scheme to make a new class of MEMS sensors and actuators. Because the electrostatic force is modified in this method, it can be considered in the third category of methods to address the pull-in instability. Another advantage of the repulsive approach is the flexibility in increasing the voltage on the side electrodes several orders of magnitudes higher than voltages used in conventional MEMS devices based on two electrodes.

The accelerometer in this paper is fabricated with the POLYMUMPs standard and tested with a mechanical shaker. The proof mass and substrate velocities are measured with a laser vibrometer to extract the relative motion between the two. An electrical circuit is designed to measure the electrical output of the accelerometer. The accelerometer has a translational degree of freedom which allows for detecting and measuring acceleration along 1-axis. The rest of this paper is organized as follows. Section II presents the fabrication and the working principle of the accelerometer. In Section III we present a mathematical model of the accelerometer to study its response under electrostatic and mechanical loads. Section IV introduces the electrical circuit that is used to detect the output of the device. The experimental results are presented and discussed in section V. Finally, the conclusion is given in section VI.

II. Fabrication and Working Principle of the Accelerometer

The schematic of the fabricated accelerometer is shown in Fig. 2 (a). The dimensions of the accelerometer is given in Table I. The accelerometer has a square proof-mass that employs 27 repulsive electrodes on each side of it. The accelerometer is suspended above the substrate with four serpentine springs at its corners. Figure 1 illustrates the principle of operation for the accelerometer. By applying voltage on the side electrodes, the accelerometer is pushed away from the substrate to a static equilibrium point. If an acceleration is applied along the z axis, which is the sense axis of the accelerometer, the proof mass will experience a dynamic motion relative to its substrate. This motion leads to a capacitance change between the moving and side electrodes, which can be sensed with an electrical circuit. Therefore, by measuring the change in capacitance between the moving and side electrodes the applied acceleration could be measured.

The accelerometer is built using the POLYMUMPs fabrication standard. This standard allows for three structural layers, poly0, poly1, and poly2. The fabricated accelerometer is shown in this Fig. 2 (b). The fixed electrodes are built in the poly0 layer and they are all connected to each other through a square plate that is underneath the proof-mass. The proof-mass and all the moving electrodes that are

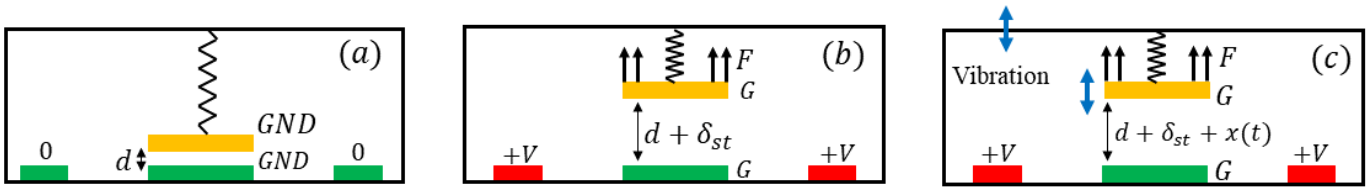

Fig. 1. The principle of operation for the accelerometer. (a) ($V_{dc} = 0$). (b) ($V_{dc} \neq 0$). (c) ($V_{dc} \neq 0$) and acceleration is applied.

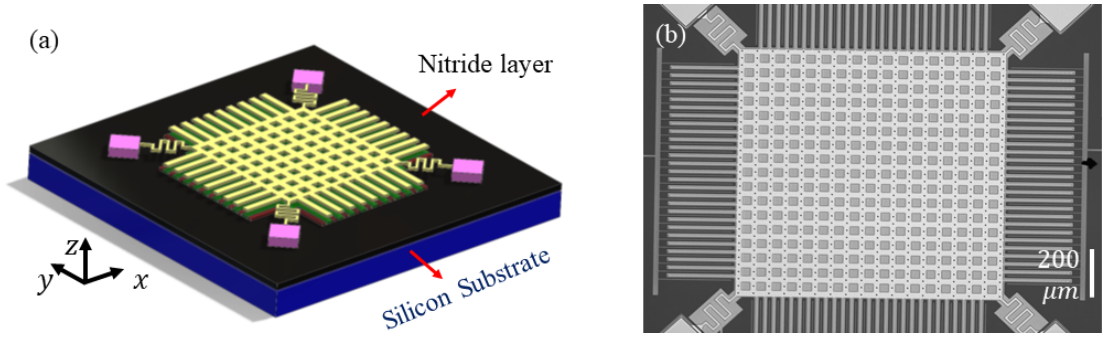

Fig. 2. (a) The 3D schematic of the accelerometer. (b) The fabricated accelerometer based on the POLYMUMPs standard

TABLE I
DIMENSIONS FOR THE MICROSTRUCTURE IN FIGURE 2.

Parameter	Symbol	Value
Plate length (μm)	L	1000
Plate width (μm)	L	1000
Moving electrode length (μm)	L_b	250
Total number of electrode sets	N	108
Moving electrode width (μm)	-	6
Side electrode width (μm)	-	4
Bottom electrode width (μm)	-	16
Gap between side and bottom electrodes (μm)	-	6
Moving electrode thickness (μm)	-	1.5
Bottom and side electrode thickness (μm)	-	0.5
Initial gap between moving and bottom electrodes (μm)	d	2.75
Mass of the microstructure (kg)	m	3.0269×10^{-9}
Simulated natural frequency ($\frac{rad}{s}$)	ω_{nSim}	10078
Experimental natural frequency ($\frac{rad}{s}$)	ω_n	7037
Constant damping ratio	ζ_0	0.0077
Linear damping ratio	ζ_1	0.2336
Modulus of elasticity (Gpa)	E	160
Density ($\frac{kg}{m^3}$)	–	2330
Force coefficient	A_0	6.9534×10^{-8}
Force coefficient	A_1	1.65×10^{-2}
Force coefficient	A_2	-6.7048×10^{3}
Force coefficient	A_3	6.6876×10^{8}
Force coefficient	A_4	-1.5849×10^{13}
Force coefficient	A_5	-1.9187×10^{18}
Force coefficient	A_6	1.8163×10^{23}
Force coefficient	A_7	-6.8752×10^{27}
Force coefficient	A_8	1.2715×10^{32}
Force coefficient	A_9	-9.4512×10^{35}
Spring dimension (μm)	a_1	50
Spring dimension (μm)	a_2	40
Spring dimension (μm)	b_1	45
Spring dimension (μm)	a_3	40

attached to it are made in the poly2 layer. The initial gap between the microstructure and the underneath poly0 layer is $2.75\mu m$ that is result of removing the two oxide layers. These layers are deposited on top of a silicon nitride layer which acts as an insulator. However, we have seen in the experiment that this silicon nitride layer is not a good insulator because the electrical charges could leak from the side electrodes to the bottom electrode and the moving electrode (through the anchors). It is worth mentioning that silicon dioxide is usually a better option for an insulator layer as its resistance is several orders of magnitudes higher than silicon nitride. This leakage current was very problematic and we will discuss in section IV how this problem was mitigated.

III. MATHEMATICAL MODELING

In this section, we develop a mathematical model for the accelerometer under electrostatic and mechanical loads. This model along with our previous work [4] have been used for the design of the current accelerometer before fabricating it. We model the motion of proof-mass with the one degree of freedom system shown in Fig. 3 (a). The deformations of the repulsive electrodes attached to the perimeter of the proof-mass is modeled with Euler-Bernoulli beam. The governing equations of the motion for the proof-mass and the beams are given as following.

$$EI_{xx}\frac{\partial^4 w(z,t)}{\partial z^4} + \rho A\frac{\partial^2 w(z,t)}{\partial t^2} = V_{dc}^2 F_{es}(x + w(z,t)) \quad (1)$$

$$m\ddot{x} + c\dot{x} + kx = f(x) + mg_0 sin(\omega t) \quad (2)$$

Where, $w(z,t)$ is the deflection of the beam with respect to the proof-mass. In Eq. 1, the displacement of the proof-mass is shown by x, and the electrostatic force on each beam is represented by F_{es}, which is a function of the gap between the moving and bottom electrodes. V_{dc} in Eq. 1 is the amount of

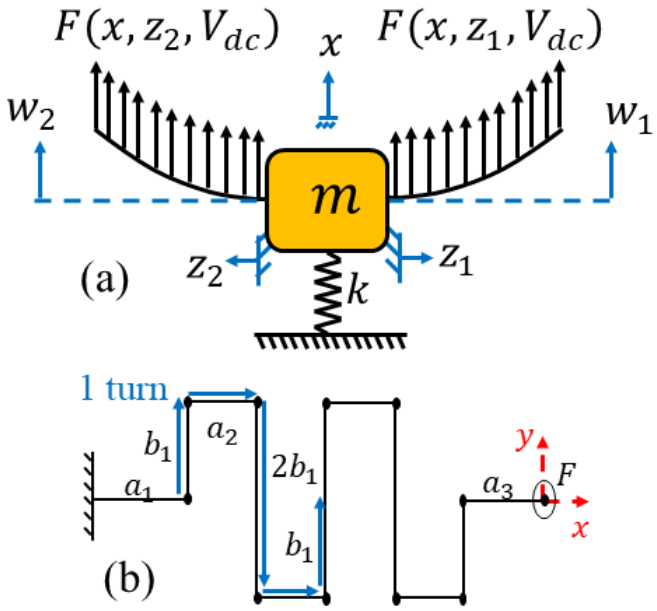

Fig. 3. (a) The mathematical model for the accelerometer. (b) One of the supporting serpentine springs. The dimensions of the spring are given in the Table I.

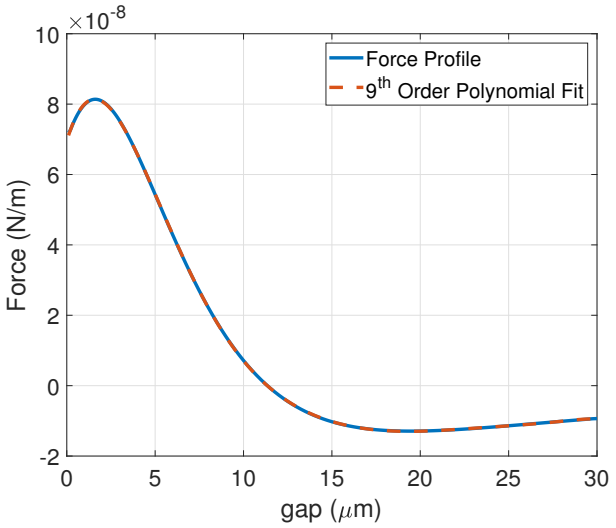

Fig. 4. The electrostatic force profile obtained from boundary element approach (when $V_{dc} = 1(V)$)and the 9^{th} order polynomial fit.

voltage applied on the side electrodes, and g_0 is the amplitude of the acceleration applied. All the other parameters in Eq. 1 are given in the Table I. $f(x)$ in Eq. 2 is the electrostatic force that is exerted on the proof-mass which is the sum of the electrostatic force on all the moving electrodes given in Eq. 3 .

$$f(x(t)) = 4 \times N \times \int_0^{L_b} F_{es}(x(t) + w(z,t))dz \qquad (3)$$

Where N is the number of electrodes on each side, and the factor 4 represents the fact that there are four sets of electrodes on the four sides of the proof-mass. The electrostatic force

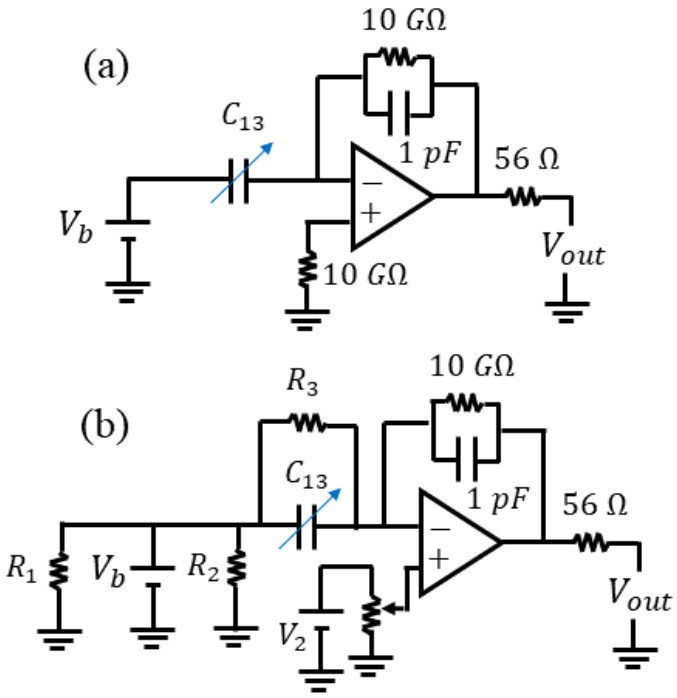

Fig. 5. (a) The original circuit designed for measuring the change in capacitance assuming there is no leakage. (b) The modified circuit to address the leakage through the nitride layer and address the op-amp saturation problem. The leakage through the nitride layer is shown with R_1, R_2,R_3 resistors.

on all the beams on one side of the proof-mass is calculated using the boundary element approach explained in [19]. For more comprehensive use of this boundary element method for repulsive configuration, one could refer to [20]. To obtain the electrostatic force on one beam, the electrostatic force should be divided by 27 because there are 27 moving electrodes on each side of the proof-mass. As mentioned, the electrostatic force is a function of gap between the moving and the bottom electrodes. The gap between these two electrodes changes along the length of the beam. The electrostatic force profile is shown in Fig. 4 as a function of gap.

Because the first natural frequency of the microbeam $(9.1(kHz))$ is well above the frequency ranges that we would test the accelerometer for (below $4(kHz)$), the beam deflection would be quasi-static. Therefore, we can ignore the inertial term in Eq. 1. We consider the mass of the moving electrodes in the total mass of the proof-mass (m). In other word, the mass (m) is equal to the mass of the plate and all the moving electrode which is given in Table I. By substitute Eq. 3 into Eq. 2, and using it along with Eq. 1, we will have two equations with two unknowns w and x as following.

$$EI_{xx}\frac{\partial^4 w(z,t)}{\partial z^4} = V_{dc}^2 F_{es}(x + w(z,t)) \qquad (4)$$

$$\ddot{x} + 2\zeta\omega_n\dot{x} + \omega_n^2 x = \frac{4N}{m}\int_0^{L_b} F_{es}(x + w(z,t))dz + g_0 sin(\omega t) \qquad (5)$$

Where, ζ and ω_n are the damping ratio and the natural frequency of the spring-mass system respectively. We obtained an estimate for the mechanical natural frequency of the device by calculating the mass and stiffness of the microstructure. The stiffness of the serpentine springs were calculated using Castigliano's theorem [21]. The geometry of the serpentine spring is shown in Fig. 3 (b). The simulated value of the mechanical natural frequency was calculated to be $1604(Hz)$. Our expectation for the natural frequency of the fabricated devices is to be less than this value, because this model considers the proof-mass as a rigid body and does not account for its flexibility (finite stiffness). The natural frequency of the microstructure and the damping ratios are identified from the experiment after the fabrication, which are presented in the Table I. Because of squeeze film effects, the damping ratios depend on the frequency [3]. Because by changing the voltage on the side electrodes the resonance frequency of the system would change, the damping ratios would depend on the voltage. The damping ratios are given in the Table I. The total displacement can be written as:

$$x(t) = x_d(t) + x_{st} \tag{6}$$

Where $x_d(t)$ is the amplitude of dynamic motion about the equilibrium point caused by base excitation, and x_{st} is the static deflection due to electrostatic force at a given voltage. The static deflection can be obtained by setting time-varying terms equal to zero in Eq. 4 and Eq. 5.

We have used the bvp4c command in MATLAB and the shooting method [3], [15] to solve the static and dynamics equations numerically. In Section V, where we present the experimental results, the simulation result are presented as well.

IV. Electrical Circuit

In order to measure the change in capacitance between the side electrodes and the moving electrode, we have built an electrical circuit with surface mount components which is shown in Fig. 5 (a). In this circuit, we have made a charge amplifier with an operational amplifier (op-amp). The variable capacitor C_{13} denotes the capacitance between the side electrode and the moving electrode. However, as we mentioned in the Section II, we realized that there is charge leakage through the nitride layer. This leakage could be considered as resistor between the bottom electrodes and side electrodes, between the bottom electrodes and the moving electrodes, and between the side electrodes and the moving electrodes. These resistances are shown with R_1, R_2, and R_3 in Fig. 5 (b) respectively. With the leakage from the side to the moving electrodes, applying a voltage on the side electrodes leads to a charge on the moving electrodes. This charge leads to the existence of an electrical voltage on the inverting input of the op-amp that is much greater the allowed voltage difference between the inputs of the op-amp before running the op-amp to the saturation region. For a side electrode bias voltage of 72 (V), this voltage is measured to be around 17 (mV).

In order to address this issue, we considered the circuit shown in Fig. 5 (b). As is shown in this figure, the non-inverting input of the op-amp is no longer connected to ground. Instead we have used a voltage divider to generate a voltage that is equal to the voltage on the inverting input, and therefore canceling it out. It is worth mentioning that the op-amp multiplies the voltage difference between its input by a very large gain. If the voltage difference between the inputs of the op-amp is large, that would cause the op-amp to enter its saturation region which is not desirable. By having the voltage divider, we can make the voltage difference between the inputs of the op-amp nearly zero. This would allow the op-amp to operate in its linear range, which enables us to measure the capacitance change due to dynamic motion of the proof mass.

V. Experimental Results

In this section, the experimental setup that is used to measure the mechanical and electrical responses of the accelerometer is explained. Then, the experimental results for different electrical voltages and mechanical excitation are presented.

The acceleromter and the shaker are placed inside a vacuum chamber having its pressure is controlled by a pressure controller set. Since this is our first attempt to investigate the electrical read-out of the accelerometer, we have tested it at reduced pressures to make sure the accelerometer would have enough large motion to generate an electrical signal. In a future extension of this work, the accelerometer could be tested in atmospheric pressure. Figure IV (a) shows the accelerometer chip mounted on the printed circuit board (PCB) with ultra-violet (UV) cured epoxy. Figure IV (b) shows the schematic of the experimental setup. The PCB is attached to a fixture, and then it is mounted on top of a mechanical shaker. We use the shaker to perform a frequency sweep while keeping the amplitude of the acceleration constant. In order to apply a constant acceleration at different frequencies, first, we need to characterize the performance of the shaker inside the vacuum chamber. For the shaker characterization, the laser vibrometer is focused on the substrate to measure its velocity. For any amplitude of the acceleration (for example, 1g where g is the gravitational acceleration of Earth), the frequency is swept from $600Hz$ to $4(kHz)$. At each frequency, we run a loop to send voltages with different amplitudes to the shaker. If the acceleration of the substrate is within the 1% range of the desired value (here between 0.99g and 1.01g) then the value of the voltage that is sent to the shaker is recorded for that frequency to generate the desired acceleration (1g).

After characterizing the shaker for different g-levels, we apply a desired voltage on the side electrodes and then perform a backward frequency sweep. The laser vibrometer is used again to measure the motion of the accelerometer proof mass relative to the substrate by measuring their velocities. To calculate the relative motion, the experiment is performed twice for each load case scenario. In the first measurement, the laser vibrometer is focused on the substrate to measure

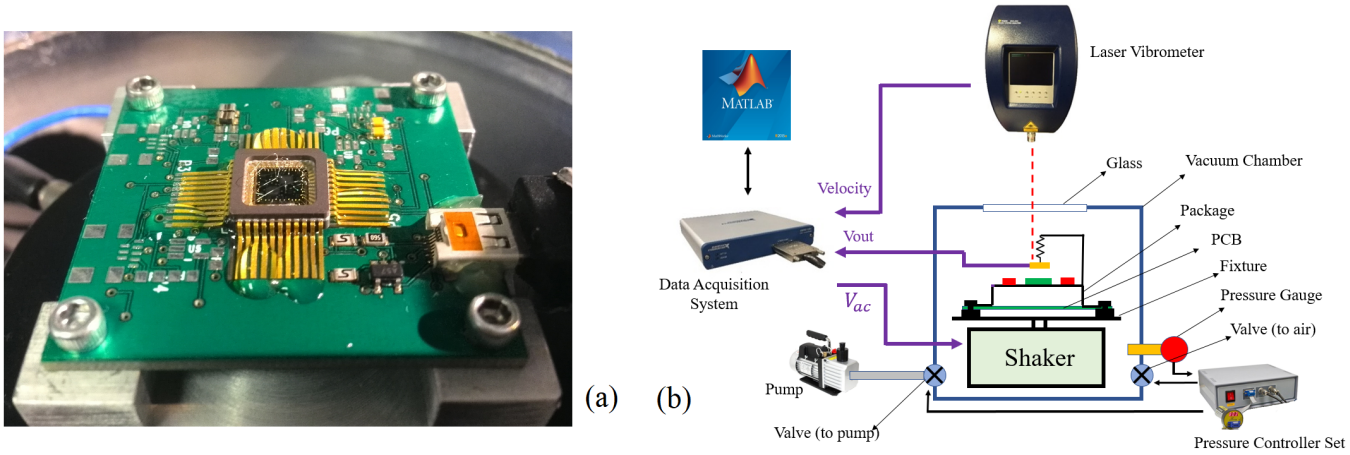

Fig. 6. (a)The chip mounted on the PCB which itself is mounted on the shaker. (b) The experimental setup

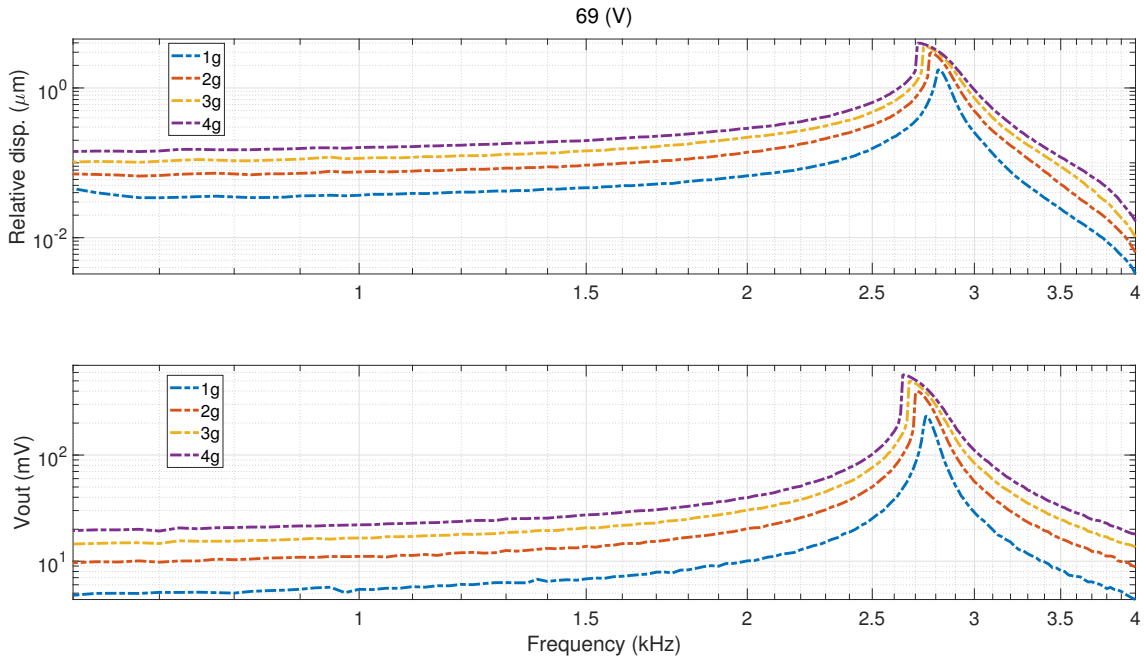

Fig. 7. The experimental displacement and readout voltage data for different excitation level when the voltage on side electrodes is 69 (V)

its velocity. In the second measurement, the laser vibrometer is focused on the center point of the proof mass to measure its velocity at each frequency. By performing a least squares analysis on the velocity data, the relative displacement of the proof mass is determined.

To measure the electrical output of the accelerometer at each g-level while the frequency being swept, we run the experiment for a third time. With the data acquisition system used in these measurements, we found that reading the velocity and electrical output in one measurement led to cross-talk between the channels of the data acquisition system, which is not desirable. This is why we have done one measurement at a time. The displacement data and the electrical output of the accelerometer is presented in Fig. 7, 8, and 9 for three different voltages. At each voltage, the accelerometer is excited at several g-levels. The frequency step is considered to be $10(Hz)$ inside the resonance region and $25(Hz)$ outside the resonance region. As is shown in these figures, the accelerometer electrical output follows the same pattern as its displacement, which is promising.

The accelerometer is capable of producing an electrical output as high as 600 (mV) when it is subjected to $5g$ harmonic base excitation and the voltage on the side electrode is $78(V)$. The frequency range for operation of accelerometers is usually considered to be 1/3 of their resonance frequency. In this region, the relative displacement experienced by the proof-mass is proportional to the acceleration of the base regardless of the frequency of excitation, which enables an accurate measurement of the acceleration. The electrical sensitivity of the accelerometer is calculated by

TABLE II
THE EXPERIMENTAL RESULTS FOR THE FABRICATED ACCELEROMETER.

Voltage	69 (V)	78 (V)	95 (V)
V_{out} at 1g and 800 (Hz) - (mV)	5.01	3.42	1.97
V_{out} at 2g and 800 (Hz) - (mV)	10.33	6.85	4.11
Resonance frequency (KHz)	2.75	3.04	3.41
Maximum (V_{out}) at 1g - (mV)	232.4	182.8	129
Sensitivity - (mV/g)	5.32	3.43	2.14
Bandwidth - (kHz)	0.92	1.01	1.14

measuring its electrical output off the resonance region (at 800 (HZ)) for 1g and 2g excitation levels. At $69(V)$, the electrical sensitivity is measured to be $5.32(mV/g)$. The sensitivity, resonance frequency, and frequency range of the accelerometer for different voltages are given in table II.

The electrical sensitivity of the accelerometer decreases with an increase in the voltage on the side electrodes. We believe this is because of the leakage of charge through the nitrite layer. Our expectation for the sensitivity was to increase with the voltage on the side electrodes. In a different publication of our research group [18], where the repulsive electrode configuration is used to make a MEMS microphone, the sensitivity increases with the voltage on the side electrode. In that study, where the same electrical circuit (Fig. 5 a) is used to measure the change in capacitance, oxide is used as the insulator layer instead of nitride. For that device, we measured the voltage on the inverting input of the op-amp when a voltage is applied on the side electrode. This voltage was almost $0(V)$ as opposed to the $17(mV)$ that we measured for the accelerometer. This is why we believe the leakage through the nitrite is responsible for decrease in sensitivity. The leakage in the nitride layer of MUMPS process has been reported in [22]. The bandwidth of the accelerometer is tunable with the voltage on the side electrode. By increasing the voltage on the side electrodes, the resonance frequency of the microstructure increases. This leads to a larger bandwidth in which the frequency response is flat. For instance, when the voltage is increased from $69(V)$ to $95(V)$ (a 37% increase), the resonance frequency increases from $2820(Hz)$ to $3420(Hz)$ (21% increase). The increase in the natural frequency means that the device gets more stiff and this translates to the displacement of the proof-mass at a certain g-level being smaller as the voltage increases. Thus, there is a trade off between electrical sensitivity and mechanical stiffness. As the voltage increases, the electrical sensitivity increases but the mechanical sensitivity decreases.

The softening nonlinear behavior near resonance region shown in Fig.7, 8, and 9 is a characteristic of the electrostatic force in repulsive schemes. However, the resonance frequency increases as the voltage on the side electrodes increases (see Table II). This is because the contribution of the electrical stiffness in the total stiffness of the microstructure (mechanical + electrical) increases by increase in the voltage on the side electrodes. Even though the repulsive electrode configuration provides flexibility to increase the voltage on the side electrodes, it should be mentioned that the voltage on the side electrodes can not be increased infinitely in practice. This is because the microstructure has a finite stiffness in the lateral direction, which means that if the voltage is increased without a limit, the moving electrode will eventually collapse to the side electrodes. However, this limit is substantially higher compared to the pull-in voltage in conventional MEMS devices based on two electrodes [20]. For example, the current accelerometer has been tested at $95(V)$ without exhibiting pull-in failure. As a comparison, if the current accelerometer employs conventional parallel-plate electrode configuration, the pull-in voltage would be $0.8(V)$ according to Eq. 7 [3]. In other words, if the bias voltage is applied between the moving and bottom electrodes (side electrodes grounded), then the accelerometer will suffer from pull-in at $0.8(V)$. According to our previous study, the lateral pull-in for the accelerometer happens around $120(V)$.

$$V_{pull-in} = \sqrt{\frac{8m\omega_n^2 d^3}{27\epsilon_0 A}} = \sqrt{\frac{8 \times 3.0269 \times 10^{-9} \times 7037^2}{27 \times 8.85 \times 10^{-12} \times 4 \times 27 \times 250 \times 10^{-6} \times 6 \times 10^{-6}}} = 0.8(V) \quad (7)$$

Figure 10 shows the results of the mathematical model, which was developed in Section III, and compare them with experimental results. We have presented the results at lowest and highest g-level at each voltage. As Fig. 10 illustrates, there is a good agreement between the simulation and experimental results. The one degree of freedom model of the complicated microstructure captures the amplitude in frequencies lower than resonance (This region is used to derive the sensitivity of the device), and even in resonance region. It also captures the resonance frequency and the bandwidth of the resonance peak in the experiment with acceptable accuracy (the largest mismatch between the resonance frequency is 1.8% that happens at $95V - 1g$). The stroke of conventional capacitive accelerometer devices is limited to the initial gap because the travel direction can only be towards the substrate. A comparison between the performance characteristics of the proposed accelerometer in this study with the accelerometers in the literature is given in the Table III.

VI. CONCLUSION

A capacitive MEMS accelerometer based on the repulsive electrode configuration is fabricated and tested in this study. An electrical circuit was built to measure the electrical output of the accelerometer. The mechanical response of the accelerometer is measured with a laser vibrometer. The accelerometer responses to several base excitation g-levels and at different voltages applied to the side electrodes are presented. While the initial fabrication gap is $2.75\mu m$, the accelerometer can reach $4.2\mu m$ dynamical displacement amplitude. This study shows the successful performance of

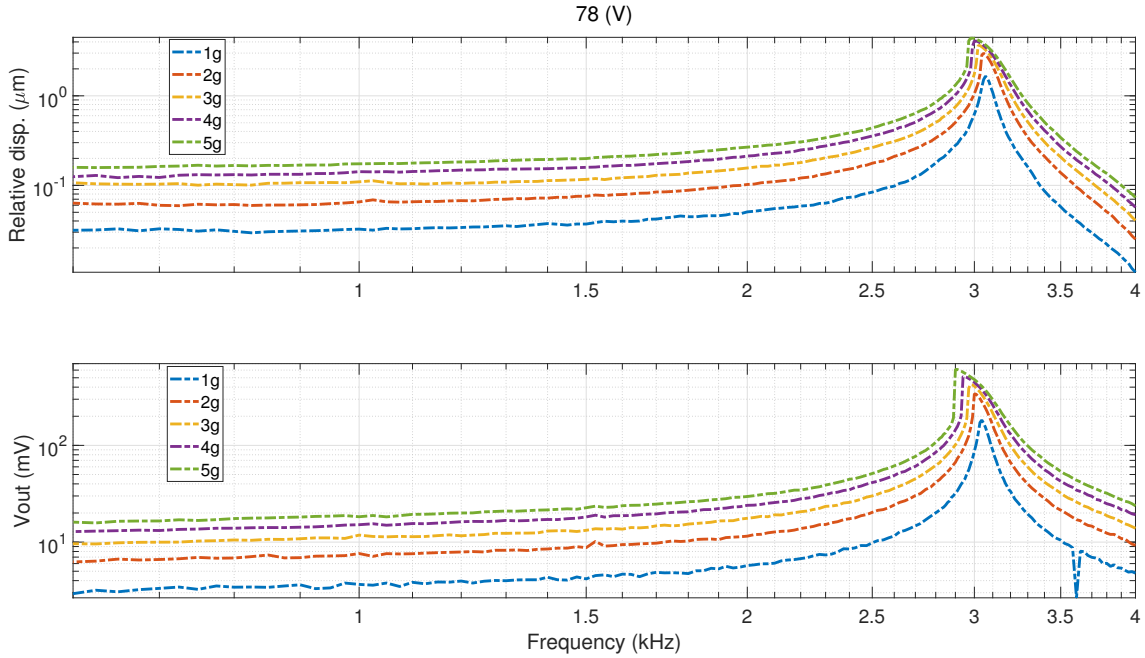

Fig. 8. The experimental displacement and readout voltage data for different excitation level when the voltage on side electrodes is 78 (V)

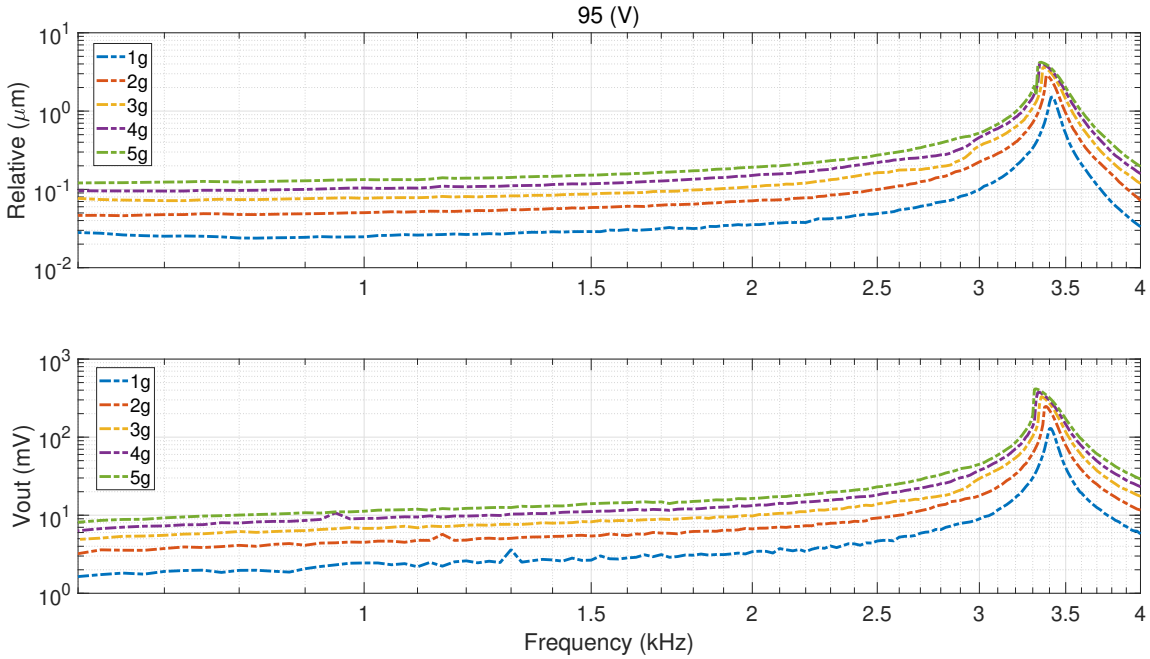

Fig. 9. The experimental displacement and readout voltage data for different excitation level when the voltage on side electrodes is 95(V)

the accelerometer when it is subjected to a voltage on the side electrodes as high as $95(V)$ without suffering from pull-in instability. The accelerometer output voltage is proportional to the base acceleration. The accelerometer has a mechanical sensitivity of $35\frac{nm}{g}$ and electrical sensitivity of $5.3\frac{mV}{g}$. The frequency range of the acceleromter is tunable with the voltage on the side electrode, making it suitable for use in different applications and environments.

References

[1] L. Roylance and J. Angell, "A miniature integrated circuit accelerometer," *1978 IEEE Int. Solid-State Circuits Conf, San Francisco, CA, USA, pp. 220–221.*

[2] H. Xie, G. K. Fedder, and R. E. Sulouff, *2.05 - Accelerometers*, Y. B. Gianchandani, O. Tabata, and H. Zappe, Eds. Oxford: Elsevier, 2008.

[3] M. I. Younis, *MEMS Linear and Nonlinear Statics and Dynamics*. Springer, New York, 2011.

[4] M. Daeichin, M. Ozdogan, S. Towfighian, and R. N. Miles, "Dynamic response of a tunable mems accelerometer based on repulsive force," *Sensors & Actuators: A. Physical*, 2019.

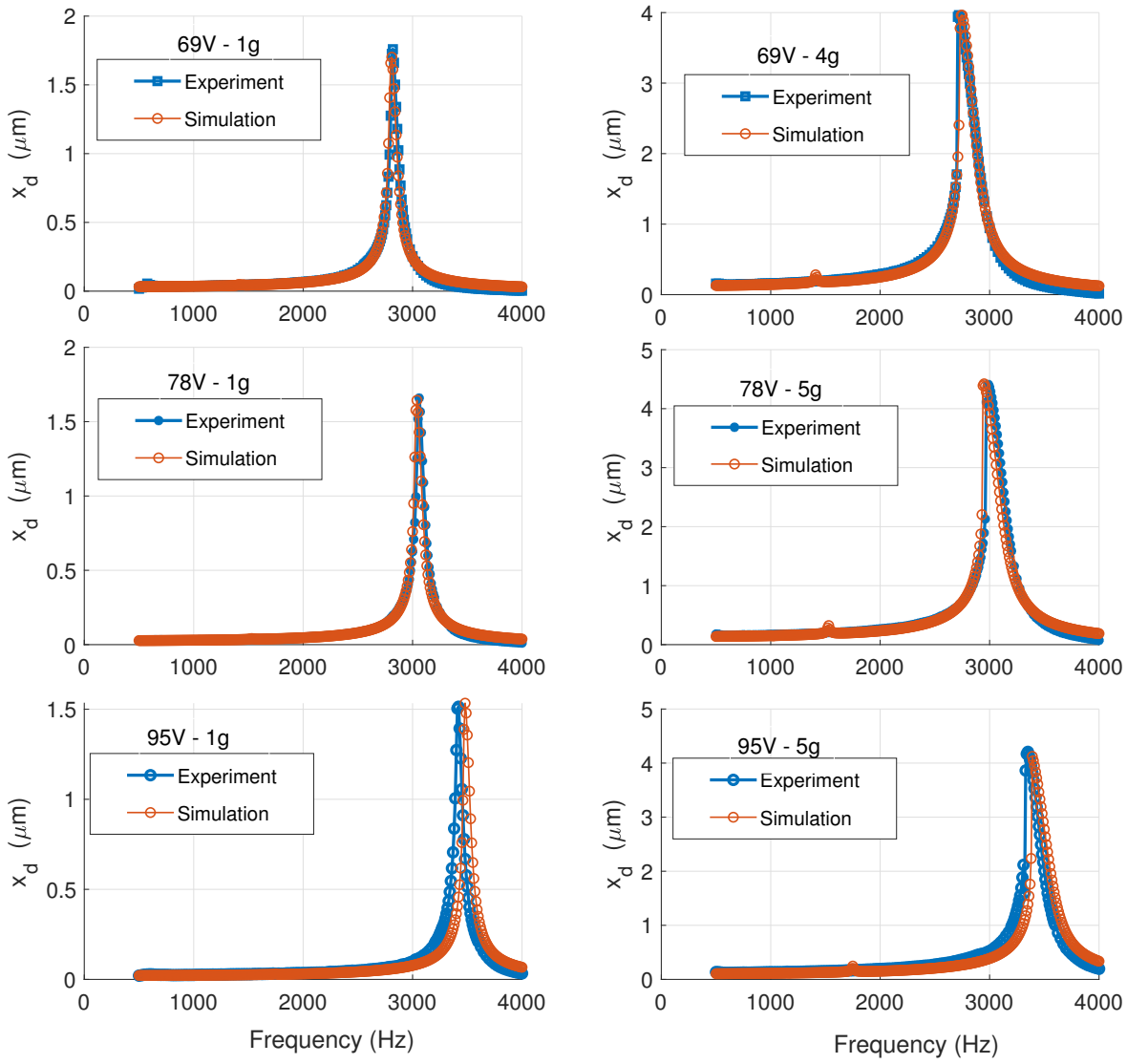

Fig. 10. Experimental results versus simulation results

[5] L. Ristic, R. Gutteridge, B. Dunn, D. Mietus, and P. Bennett, "Surface micromachined polysilicon accelerometer," *Technical Digest IEEE Solid-State Sensor and Actuator Workshop, Hilton Head Island, SC, USA, 1992, pp. 118-121.*

[6] W. Zhang, H. Yan, Z.-K. Peng, and G. Meng, "Electrostatic pull-in instability in mems/nems: A review," *Sensors and Actuators A: Physical*, vol. 214, pp. 187 – 218, 2014.

[7] M. Ozdogan, M. Daeichin, A. Ramini, and S. Towfighian, "Parametric resonance of a repulsive force mems electrostatic mirror," *Sensors and Actuators A: Physical*, vol. 265, 2017.

[8] B. Rivlin and D. Elata, "Design of nonlinear springs for attaining a linear response in gap-closing electrostatic actuators," *International Journal of Solids and Structures*, vol. 49, no. 26, pp. 3816 – 3822, 2012.

[9] Jinghong Chen, W. Weingartner, A. Azarov, and R. C. Giles, "Tilt-angle stabilization of electrostatically actuated micromechanical mirrors beyond the pull-in point," *Journal of Microelectromechanical Systems*, vol. 13, no. 6, pp. 988–997, 2004.

[10] J. I. Seeger and S. B. Crary, "Stabilization of electrostatically actuated mechanical devices," in *Proceedings of International Solid State Sensors and Actuators Conference (Transducers '97)*, vol. 2, pp. 1133–1136 vol.2, 1997.

[11] J. I. Seeger and B. E. Boser, "Charge control of parallel-plate, electrostatic actuators and the tip-in instability," *Journal of Microelectromechanical Systems*, vol. 12, no. 5, pp. 656–671, 2003.

[12] R. Nadal-Guardia, A. Dehe, R. Aigner, and L. M. Castaner, "Current drive methods to extend the range of travel of electrostatic microactuators beyond the voltage pull-in point," *Journal of Microelectromechanical Systems*, vol. 11, no. 3, pp. 255–263, 2002.

[13] E. S. Hung and S. D. Senturia, "Extending the travel range of analog-tuned electrostatic actuators," *Journal of Microelectromechanical Systems*, vol. 8, no. 4, pp. 497–505, 1999.

[14] Ki Bang Lee and Young-Ho Cho, "Laterally driven electrostatic repulsive-force microactuators using asymmetric field distribution," *Journal of Microelectromechanical Systems*, vol. 10, no. 1, pp. 128–136, Mar. 2001.

[15] M. Pallay, M. Daeichin, and S. Towfighian, "Dynamic behavior of an electrostatic mems resonator with repulsive actuation," *Nonlinear Dynamics*, vol. 89, no. 2, 2017.

[16] M. Daeichin, R. N. Miles, and S. Towfighian, "Experimental characterization of the electrostatic levitation force in mems transducers," *Journal of Vibration and Acoustics*, 2020.

[17] M. Pallay and S. Towfighian, "A reliable mems switch using electrostatic levitation," *Applied Physics Letter*, 2018.

[18] M. Ozdogan, S. Towfighian, and R. N. Miles, "Modeling and characterization of a pull-in free mems microphone," *IEEE Sensors Journal*, 2020.

References	Fabrication Gap	Stroke	Resonance Frequency	Mechanical Sensitivity	Electrical Output	Pull-in Voltage	MEMS die Area	Axis	g range
[23]	$2\mu m$	$\leq 2\mu m$	$f = 3(kHz)$	–	$42.5\frac{fF}{g}$	–	$5 \times 5mm^2$	1	$\pm 1g$
[24]	$1.8\mu m$	$\leq 1.8\mu m$	$f = 2.2(kHz)$	–	$0.24\frac{V}{g}$	–	$3.2 \times 3.2mm^2$	1	$\pm 1g$
[25]	$2\mu m$	$\leq 2\mu m$	$f = 1.79(kHz)$	$8.2\frac{nm}{g}$	–	$3.5V$	$\approx 0.3 \times 0.35mm^2$	1	$\pm 10g$
[26]	Simulation $2\mu m$ Experiment $4\mu m$	$\leq 2 - 4\mu m$	$f = 1.3(kHz)$	–	$0.038\frac{pF}{g}$	Simulation $3.5V$ Experiment –	$1.5 \times 1.5mm^2$	1	$\pm 1g$
[27]	$2\mu m$	$\leq 2\mu m$	$f = 1.5(kHz)$	–	$21.3\frac{mV}{g}$	–	$2.6 \times 2mm^2$	1	$\pm 1g$
[28]	$2\mu m$	$\leq 2\mu m$	$f_x = 1.4(kHz)$ $f_y = 1.4(kHz)$ $f_z = 1.7(kHz)$	–	–	–	$12 \times 7mm^2$	3	x: $\pm 10g$ y: $\pm 10g$ z:$+12/-7g$
This study	$2.75\mu m$	$4.2\mu m$	$f = 1.12(kHz)$	$35\frac{nm}{g}$	$5.3\frac{mV}{g}$	$> 95V$	$1.4 \times 1.4mm^2$	1	$\pm 5g$

TABLE III

COMPARISON OF PRESENT ACCELEROMETER WITH THOSE REPORTED IN THE LITERATURE. THE DASH ENTRY MEANS THAT THE NUMBER IS NOT GIVEN.

[19] R. N. Miles, *Physical Approach to Engineering Acoustics (in press)*. Springer, New York, 2019.

[20] M. Daeichin, R. N. Miles, and S. Towfighian, "Lateral pull-in instability of mems transducers employing repulsive force," *Nonlinear Dynamics*, 2020.

[21] F. P. Beer, E. R. J. Jr., J. T. DeWolf, and D. F. Mazurek, *Mechanics of materials*. New York: McGraw-Hill Higher Education, 2009.

[22] H. R. Shea, A. Gasparyan, H. B. Chan, S. Arney, R. E. Frahm, D. López, S. Jin, and R. P. McConnell, "Effects of electrical leakage currents on mems reliability and performance," *IEEE Transactions on Device and Materials Reliability*, vol. 4, no. 2, pp. 198–207, 2004.

[23] C.-P. Hsu, M.-C. Yip, and W. Fang, "Implementation of a gap-closing differential capacitive sensingZ-axis accelerometer on an SOI wafer," *Journal of Micromechanics and Microengineering*, vol. 19, no. 7, p. 075006, Jun. 2009.

[24] X. Zhou, L. Che, S. Liang, Y. Lin, X. Li, and Y. Wang, "Design and fabrication of a mems capacitive accelerometer with fully symmetrical double-sided h-shaped beam structure," *Microelectronic Engineering*, vol. 131, pp. 51 – 57, 2015.

[25] P. Kachhawa and R. Komaragiri, "Performance optimization of mems capacitive accelerometer," in *2014 International Conference on Devices, Circuits and Communications (ICDCCom)*, pp. 1–5, 2014.

[26] I. Lee, G. H. Yoon, J. Park, S. Seok, K. Chun, and K.-I. Lee, "Development and analysis of the vertical capacitive accelerometer," *Sensors and Actuators A: Physical*, vol. 119, no. 1, pp. 8 – 18, 2005.

[27] H. Zhang, X. Wei, Y. Ding, Z. Jiang, and J. Ren, "A low noise capacitive mems accelerometer with anti-spring structure," *Sensors and Actuators A: Physical*, vol. 296, pp. 79 – 86, 2019.

[28] S. Tez, U. Aykutlu, M. M. Torunbalci, and T. Akin, "A bulk-micromachined three-axis capacitive mems accelerometer on a single die," *Journal of Microelectromechanical Systems*, vol. 24, no. 5, pp. 1264–1274, 2015.

Meysam Daeichin received his Master's degree in Mechanical Engineering from Sharif University of Technology in 2013. He started his PhD program in Mechanical Engineering at SUNY Binghamton in 2015, and is currently working toward earning his degree. His research interests include MEMS sensors and actuators, nonlinear dynamics and vibration and applied mathematics.

Ronald N. Miles received the B.S. degree in electrical engineering from the University of California at Berkeley, Berkeley, CA, USA, and the M.S. and Ph.D. degrees in mechanical engineering from the University of Washington. He has been with the Department of Mechanical Engineering, SUNY Binghamton, Binghamton, NY, USA,since 1989, and has served as the Director of Graduate Studies, Director of Undergraduate Studies, Associate Chair, Professor, Distinguished Professor, Associate Dean for Research of the Department of Mechanical Engineering.

Shahrzad Towfighian received her MS degree from Ryerson University in 2006 and her PhD degree in Mechanical Engineering from the University of Waterloo,Canada in 2011. She joined the Mechanical Engineering department at Binghamton University in Fall 2013. Her research interests include Micro-electro-mechanical sensors/actuators and energy harvesting. She develops mathematical modeling of electro-mechanical systems to study nonlinearities and their effect on the system performance. She discovers new ways of sensing and actuation for improving functionality of MEMS devices.